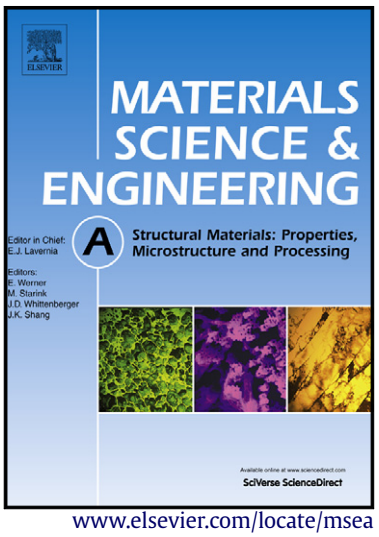

www.elsevier.com/locate/msea

Effect of age hardening on the deformation behavior of an Mg-Y-Nd alloy: In-situ X-ray diffraction and crystal plasticity modeling

Martin Lentz, Manuela Klaus, Michael Wagner, Christoph Fahrenson, Irene J. Beyerlein, Milovan Zecevic, Walter Reimers, Marko Knezevic

PII: S0921-5093(15)00096-9
DOI: http://dx.doi.org/10.1016/j.msea.2015.01.069
Reference: MSA32007

To appear in: *Materials Science & Engineering A*

Cite this article as: Martin Lentz, Manuela Klaus, Michael Wagner, Christoph Fahrenson, Irene J. Beyerlein, Milovan Zecevic, Walter Reimers, Marko Knezevic, Effect of age hardening on the deformation behavior of an Mg-Y-Nd alloy: In-situ X-ray diffraction and crystal plasticity modeling, *Materials Science & Engineering A,* http://dx.doi.org/10.1016/j.msea.2015.01.069

Effect of age hardening on the deformation behavior of an Mg-Y-Nd alloy: In-situ X-ray diffraction and crystal plasticity modeling

Martin Lentz[a,*], Manuela Klaus[b], Michael Wagner[a], Christoph Fahrenson[c], Irene J. Beyerlein[d], Milovan Zecevic[e], Walter Reimers[a], Marko Knezevic[e]

[a]Technische Universität Berlin, Metallische Werkstoffe, Ernst-Reuter-Platz 1, 10587 Berlin, Germany
[b]Helmholtz-Zentrum Berlin für Materialien und Energien, Albert-Einstein-Straße 15, 12489 Berlin, Germany
[c]Technische Universität Berlin, Zentraleinrichtung Elektronenmikroskopie, Straße des 17. Juni 135, 10623 Berlin, Germany
[d]Los Alamos National Laboratory, Theoretical Division, Los Alamos, NM 87545, USA
[e]University of New Hampshire, Department of Mechanical Engineering, Durham, NH 03824, USA

* corresponding author: Phone: ++49 30 314-22381, fax: ++49 30 314-22996, martin.lentz@tu-berlin.de

Abstract

The present study investigates the deformation behavior of an extruded Mg-Y-Nd (WE54) alloy in as-extruded and aged conditions. Via age-hardening at 250 °C for 16 and 500 hours or annealing treatments at 400 °C for 24 hours, precipitates are formed within the grains or at the grain boundaries. To characterize microstructural changes with the age-hardening conditions, we employ electron-backscattered diffraction, transmission electron microscopy, and optical microscopy. In the as-extruded material, we observed an uncommonly low activity of $\{10\bar{1}2\}\langle 10\bar{1}\bar{1}\rangle$ tension twinning in comparison with other Mg alloys. The tension twinning activity substantially increased after precipitation hardening and the accompanying reduction of alloying element concentration in solid solution. Consistent with the microstructural observations, the increase in twin activity clearly manifests in the compression flow curves. While the as-extruded and 16-hour/250 °C samples exhibited a classical decreasing hardening rate throughout straining associated with crystallographic slip, the 500-hour/250 °C and the

400 °C annealed sample featured a characteristic increase in the hardening rate associated with twinning. In order to determine the impact of the different heat treatments on the individual slip and twinning modes, in-situ energy-dispersive X-ray synchrotron diffraction experiments during loading and elasto-plastic self-consistent modeling were conducted. We find that plate-shape precipitates on the $\{10\bar{1}0\}_\alpha$ planes harden <a> basal slip more than the other slip systems, while the reduced solute concentration in the 500 h 250 °C and 24 h 400 °C samples results in a significant decrease in the critical resolved shear stress for $\{10\bar{1}2\}\langle 10\bar{1}\bar{1}\rangle$ tension twinning.

Keywords
magnesium alloys, crystal plasticity, in-situ diffraction, deformation behavior, texture

1. Introduction

Mg and Mg alloys exhibit a complex deformation behavior, which involves multiple deformation modes and frequently results in pronounced plastic anisotropy (e.g. [1-2]). The most common deformation modes are <a> basal slip, <a> prismatic slip, <c+a> pyramidal slip and $\{10\bar{1}2\}\langle 10\bar{1}\bar{1}\rangle$ tension twinning (TTW-ing), where <a> basal slip and TTW-ing are usually readily activated ([2-6]). Over the past decades a variety of studies have been conducted to determine the influence of grain size [7-11], texture [8, 12-16], precipitates [17-25] and solutes [21, 26-33] on the activity of these deformation modes.

In the present study we focus on the effects of precipitates, which are formed within the grains or at grain boundaries during heat treatment, and of solutes on the mechanical properties, deformation behavior and the underlying relative activity of individual deformation modes, particularly TTW-ing. The effect of precipitation hardening on individual deformation modes may differ depending on the shape and the alignment of the precipitates with respect to lattice of the matrix. We analyze a WE54 alloy, which forms precipitate plates predominantly on the prismatic $\{10\bar{1}0\}_\alpha$ planes [24, 34-36]. The effects of other precipitate shapes and alignments on the deformation behavior of Mg alloys have been studied in detail in several prior works [18-24]. To explain the relationship, an Orowan equation was adapted in [17] to model the shear-resistance imposed by the precipitate plates and rods. There it was inferred that the prismatic precipitate plates, which are formed during age-hardening in WE alloys through the sequence: supersaturated solid solution (SSSS) → ordered Guinier-Preston zones → β'' (hexagonal prism shape) → β' (globular shape) → β_1 (prismatic plates $\{10\bar{1}0\}_\alpha$) → β

(prismatic plates) [24], were the most effective barriers to dislocations gliding on the basal plane of Mg. Robson [21] used the Orowan-based model from [24] to analyze the strengthening effect of basal plates, c-axis rods and prismatic plates on basal and prismatic slip as well as TTW-ing. He found that the prismatic plates are effective in strengthening all of these deformation modes. In [25], the effect of age-hardening on the deformation of an as-cast WE43 alloy is investigated via neutron diffraction and elasto-plastic self-consistent modeling (EPSC). They showed that <a> basal slip is significantly strengthened by prismatic plates, which are present in the peak-aged and over-aged condition samples, while <a> prismatic slip and <c+a> pyramidal slip experienced only modest strengthening. Interestingly, they further reported a possible reduction in the critical resolved shear stress (CRSS) for TTW-ing in the age-hardened samples [25]. In addition to age-hardening, solutes can potentially influence the active deformation modes. Lentz at al. [37] observed that TTW-ing is significantly hindered in an as-extruded WE54 alloy in comparison to an as-extruded ME21 alloy. While the alloying elements are predominantly retained in solid solution in the WE54 alloy, the ME21 alloy exhibits large amounts of precipitates and low solute concentrations. This difference possibly points to an important impact of the solutes Y and Nd on the TTW-ing activity. These studies indicated an important effect of precipitates and solutes on the active slip systems. However, a better understanding of these effects and their interactions is needed to exploit their full capacity through processing and alloy design.

Some studies have reported a significant impact of Y addition on the <c+a> pyramidal slip system [28, 30-33]. In one study, visco-plastic self-consistent (VPSC) simulations were employed to analyze the deformation behavior of binary Mg-Y alloys [28]. The enhanced ductility was attributed to a higher activity of <c+a> pyramidal slip. Using

transmission electron microscopy (TEM) and density functional theory (DFT) simulations, Sandlöbes et al. [31-33] analyzed pure Mg and binary solid solution Mg-Y alloys and reported an increased amount of <c+a> dislocations in Y containing alloys, where intrinsic I_1 stacking faults act as a heterogeneous source for <c+a> dislocations. In contrast, EPSC simulations of the deformation of binary Mg-Y alloys by Stanford et al. [30] reported a significant increase in the CRSS of <c+a> pyramidal slip with increasing Y concentration, which would suggest that concomitantly less <c+a> dislocations would be expected. Very recent electron backscatter diffraction (EBSD) results from Stanford et al. [38] suggested reduced TTW-ing activity and formation of $\{11\bar{2}1\}$ twins in Mg-5Y and Mg-10Y alloys. They proposed that the larger atomic radius of Y compared to Mg increases the CRSS of TTW-ing by inhibiting the atomic shuffling process, which accompanies the twinning shear of this twin mode.

Compared to Y, the effect of Nd on the deformation mechanisms in Mg alloys has not been as well studied. Herrera-Solaz et al. [39] investigated the effect of Nd addition on Mg-Mn alloys using crystal plasticity finite element simulations. While their modeling results predict increasing CRSSs of all slip modes compared to pure Mg, they particularly noted a strong increase of the CRSS of <a> basal slip. In addition the CRSS ratio of <a> basal slip/TTW-ing increased, whereas the CRSS ratios of <a> prismatic/TTW-ing and <c+a> pyramidal/TTW-ing decreased. DFT simulations by Sandlöbes et al. [40] and Zhang et al. [41] report a decrease in the stacking fault energy I_1 with Nd additions. In [32] it is suggested that I_1 stacking faults, which are bound by pyramidal partial dislocations, enable the generation of dislocations structures on pyramidal planes and act as heterogeneous sources for <c+a> pyramidal dislocations,

which in turn enhance the ductility. Based on these results Nd additions might enhance the activity similar to Y.

Here, we study the Mg-Y-Nd-mischmetal alloy called WE54. We selected this alloy because it enables high solute concentration of Y and Nd as well as the generation of precipitates within the grains and at grain boundaries. In the as-extruded condition, the alloy allows for an isolated investigation of solute hardening, whereas an annealing at 400 °C generates precipitates at grain boundaries and reduces the amount of alloying elements in solid solution. Advantageously, for these two conditions, the texture and grain size are almost unchanged. In contrast, as we show here, age hardening at 250 °C generates precipitates plates on prismatic planes within the grains, and hence enables the analysis of this precipitate morphology and alignment on individual deformation modes. As in the aforementioned works, the studies carried out in [25] and [37] indicate a significant effect of solutes and precipitates on the deformation behavior of WE series alloys, where solutes appear to hinder TTW-ing. However, these investigations did not include detailed investigations of the effect of changing solute concentrations on TTW-ing, which have been proven to be effective in hindering TTW-ing [38]. Therefore, our investigation focuses on the effect of different precipitate morphologies, densities and locations as well as solute concentrations on the individual slip and twinning modes and the macroscopic deformation behavior of an extruded and heat-treated WE54 alloy by means of EBSD, energy-dispersive X-ray synchrotron diffraction and EPSC modeling. This combined approach enabled us to interpret the microstructure development in terms of CRSSs and hardening of the deformation modes <a> basal, <a> prismatic, <c+a> pyramidal slip and TTW-ing. By applying different heat treatments we generate plate-shaped precipitates on prismatic plates (age-hardening at 250 °C) or precipitates at

grain boundaries (annealing at 400 °C). Our EBSD analysis reveals a significantly increased activity of TTW-ing after age-hardening for 500 h and annealing for 24 h at 400 °C. We confirm that plate-shaped precipitates on $\{10\bar{1}0\}_\alpha$ planes predominantly harden <a> basal slip, while the depletion of solutes via precipitation of either prismatic plates or grain boundary precipitates significantly promotes TTW-ing.

2. Materials and experiments

2.1 Material

The WE54 extrusion billet with the nominal composition of 5 wt% Y, 1.6 wt% Nd and 2.6 wt% heavy rare earth elements was obtained from Magnesium Elektron (Elektron WE54); Manchester (UK). The heavy rare earth fraction contains Yb, Gd, Dy and Er. The billet was machined to a diameter of 123 mm and 150 mm length and homogenized at 525°C for 8 h. The indirect extrusion process was carried out at the Extrusion Research and Development Center, TU Berlin using a billet temperature of 500 °C, a product speed of 1.7 m/min, an extrusion ratio 71:1 and air cooling.

2.2 Mechanical Testing

Quasi-static tension and compression tests were conducted using a universal testing machine (MTS810). The sample dimensions for the compression tests were $Ø$ = 10 mm, l_0 = 20 mm and for the tension tests $Ø$ = 8 mm, l_0 = 40 mm.

2.3 Microstructure characterization

The grain size of the samples was determined from optical microscopy (OM) using the ImageJ software [42]. Therefore, the samples were first prepared by grinding and polishing and then chemically polished with a solution of 12 ml hydrochloric acid (37

%), 8 ml nitric acid (65 %) and 100 ml ethanol. Subsequently, the samples were etched in a solution of 4.2 g picric acid, 10 ml acetic acid, 10 ml H_2O and 70 ml ethanol to reveal the grain structure.

A Zeiss DSM 982 GEMINI scanning electron microscope (SEM) equipped with an EDAX Hikari camera was used for the SEM investigation including EBSD data acquisition. In the case of SEM and EBSD samples, etching was skipped. The thin foils required for TEM analysis were prepared by cutting and mechanical polishing and electrolytically thinned using a TENOPOL-3 (Struers) and a solution of 5.3 g lithium chloride, 11.16 g magnesium perchlorate, 500 ml methanol and 100 ml 2-butoxy-ethanol. A TEM-Philips CM-30, which is equipped with a Voyager EDS-system, was used for TEM analysis applying an acceleration voltage of 250 keV. The observed precipitates were identified using the references [24, 34-35], and the fast Fourier transforms of the HR-TEM images, which were recorded using the FEI Titan 80-300 Berlin Holography Special TEM (Zentraleinrichtung Elektronenmikroskopie, TU Berlin).

2.4 In-situ X-ray diffraction

The in-situ energy-dispersive synchrotron X-ray diffraction experiments were performed at the EDDI-beamline [43] at the Berlin Synchrotron BESSY-II analyzing an energy range from 20 to 70 keV and the Bragg-angle 2θ of 9.72°. The beam-line is equipped with a tension and compression test station designed by Fa. Walter & Bai AG. The incoming beam was limited by slit systems to 1 x 1 mm². On the detector side, the beam was limited to 0.1 x 7 mm².

The dimensions of the in-situ synchrotron X-ray diffraction samples were $\emptyset$ = 7 mm, l_0 = 15 mm for compression and $\emptyset$ = 6 mm, l_0 = 36 mm for tension. Within the elastic region of the flow curves, the samples were loaded using load control, while displacement control was used within the plastic deformation regime. In order to determine the lattice strains, loading was stopped at defined load steps and diffraction patterns were recorded using an exposure time of 60 s. For the present study, we investigated the axial and transversal load strains. To this end, the samples were tilted at each load step using the tilt angle Ψ = 0° and Ψ = 89.9°. Here, it should be noted that some relaxation of the stress occurs during diffraction pattern acquisition and tilting of the sample. The elastic lattice strain evolution was calculated from the diffraction line positions using

$$\varepsilon^{hkil} = \frac{d^{hkil}}{d_0^{hkil}} - 1 = \frac{E_0^{hkil}}{E^{hkil}} - 1 \qquad (1)$$

with d^{hkil} and d_0^{hkil} being the lattice spacing at a load step and before loading, respectively, and E^{hkil} and E_0^{hkil} the corresponding diffraction line positions. The calculated elastic lattice strains are averaged values representing a subset of grains fulfilling the Bragg condition. Since we focus on the determination of load strains, E_0^{hkil} is determined by recording the diffraction pattern prior to loading. However, due to the initial texture developed by the extrusion process, E_0^{hkil} of the (0002) reflection could not be accurately measured. Therefore in order to estimate E_0^{hkil} for this reflection, an average diffraction line position was used. Diffraction patterns were recorded at 19 tilt angles (Ψ) within the angular range from 0° to 89.9° (in 5° steps). The error bars were calculated from the uncertainty in the peak fit.

3. Experimental results

3.1 Microstructure

Fig. 1 shows OM images of the initial microstructure of the as-extruded and heat-treated samples. All samples exhibit a fully recrystallized microstructure featuring comparable average grain sizes in the range from 17 µm (as-extruded) to 20 µm (24 h 400 °C). Therefore, grain size effects on the deformation behavior, which will be discussed in subsequent sections, are minimized.

Fig. 2 depicts the different states of precipitation. The as-extruded samples (Fig 2 a) contain minor amounts of Y-rich precipitates. Due to the homogenization heat treatment and high billet temperature, the alloying elements are predominantly retained in solid solution. Age-hardening at 250 °C generates precipitates within the grains, which were investigated via SEM (Fig 2 b and c) and TEM (Fig 3). Figs. 3 a and c were recorded using the <0002> zone axis, while Figs. 3 b and d were recorded using the $<11\bar{2}0>$ zone axis. As shown, the 16 h age-hardening results in the formation of prismatic plate-shaped (β_1) and globular precipitates (β'), while the 500 h age-hardened sample only contains prismatic plate-shaped precipitates (β). In contrast to the age-hardened samples, the annealed samples (24 h 400 °C) form precipitates in the grain boundaries and very few precipitates within the grains. Because of the low precipitation density within the grains, no significant precipitation hardening is expected. However, the precipitation at the grain boundaries would, at the same time, mean a reduced amount of solutes within the grains. As confirmation, line scans using electron probe microanalysis of a (1 h 400 °C) sample revealed a decreasing Nd (from 1.8 wt% to 0.8 wt%) and Y (from 5.3 wt% to 5.0 wt%) concentration within the grain interiors due to precipitation at grain boundaries. The texture of the alloys does not change significantly during the

heat treatment and will be discussed in conjunction with the texture evolution during loading in section 3.2.

3.2 Mechanical properties, deformation microstructure and texture

Fig. 4 depicts the flow curves of the investigated materials. As has been reported in [37, 44], the extrusions exhibit reduced tension-compression anisotropy compared to other Mg alloys, where the commonly reported sigmoidal shape of the compression flow curve is largely omitted. The 16 h age-hardening results in a very slight increase in strength, which is further improved through the 500 h age-hardening treatment. In contrast, 400 °C annealing causes a reduction in strength due to the reduced solute content and the slightly increased grain size.

Interestingly, the 500 h age-hardened and the 400 °C annealed sample show a more sigmoidal shaped compression flow curve. As this shape is associated to the activation of TTW-ing [1-2, 6, 45-47], the flow curves suggest an enhancement of TTW-ing through precipitation hardening or the reduction of the solute content. Below we will show via EBSD analysis that TTW-ing is indeed enhanced in these samples.

To study texture evolution, we show in Fig. 5 the EBSD measurements at different levels of strain. The initial textures are conventional, but weak, extrusion textures and were determined from large-scale EBSD maps (1800 x 700 µm², not shown). As might be expected from the compression flow curves, the textures at -5% do not show significant TTW-ing activity, which would be visible by an enhanced <0002> texture component. However, the 500 h age-hardened sample exhibits a weak intensity at the <0002> pole. Further compression results in the rotation of grains towards the <0002> texture component, which is associated to the activation of <a> basal slip and of TTW-ing. The local maxima at the <0002> pole is generated by TTW-ing, while the

maximum between the <11$\bar{2}$4> and the <11$\bar{2}$3> is generated through the gradual rotation of grains by crystallographic slip. In comparison to other Mg alloys [16, 37] the rotation towards the <0002> texture component by slip is slow, which indicates the enhanced activation of non-basal slip modes. During tensile testing the <10$\bar{1}$0> texture component is enhanced, which was explained in [37] by the activation of <a> slip systems.

The EBSD maps (Fig. 6) and the calculated misorientation distribution functions (MDF) (Fig. 7) confirm an increased TTW-ing activity in 500 h age hardened and 24 h 400 °C annealed samples. TTWs appear as red domains within their parent grains in Fig 6 a), d), g) and j). While the as-extruded (Fig. 6a) and the 16 h age hardened (Fig. 6d) samples feature a few lenticular shaped twins, the 500 h age hardened and the annealed samples contain a significantly larger area fraction of TTWs. Compared to the as-extruded and the 16 h age hardened sample, these samples have a larger number of grains containing at least one TTW, many of which contain multiple TTW lamellae and wider TTWs. The difference in TTW-ing activity is quantified statistically in Fig. 7. The relative frequency of TTW boundaries and therefore, the TTW-ing activity increases in the following order: as-extruded (Fig. 7a) < 16 h 250 °C (Fig. 7b) < 24 h 400 °C (Fig. 7d) < 500 h 250 °C (Fig. 7c). Figs. 6 b), e), h) and k) exhibit the EBSD maps of the compression samples, which were used in the in-situ energy-dispersive X-ray synchrotron diffraction experiments (final load step). All samples, but in particular the as-extruded and the 16 h age hardened samples, contain partially twinned grains at this high strain level. Hence, TTW-ing proceeds uncommonly slow compared to other Mg alloys, where TTWs grow readily and overtake the parent grains quickly [37, 45, 48, 49], as has been reported in [37]. Figs. 6 c), f), i) and l) exhibit the EBSD maps of

the tension samples (final load step). During tensile loading, negligible amounts of twins are generated, and the grains predominantly feature a <$10\bar{1}0$> orientation.

4. Modeling framework

To analyze the effect of the precipitates and solutes on the deformation modes common to Mg alloys: <a> basal slip, <a> prismatic slip, <c+a> pyramidal slip and TTW-ing, we combine in-situ energy-dispersive X-ray synchrotron diffraction during loading and elasto-plastic self-consistent modeling (EPSC). The EPSC model calculates the flow curves as a result of elastic and plastic deformation due to slip and twinning, and the underlying texture evolution as well as elastic lattice strains and the relative contributions of slip and twinning. The in-situ X-ray diffraction experiments allow for the determination of internal elastic lattice strains from changes in the diffraction line position (eq. 1), which are linked to texture evolution and the activity of deformation modes. The lattice strains determined from this technique are averaged elastic lattice strains within a subset of grains, which fulfill the Bragg condition for a predefined orientation. The mean-field EPSC model is capable of predicting the average elastic lattice strains of a similar group of grains from the polycrystal. Hence, in addition to the average stress-strain response and texture evolution, the elastic lattice strains provide additional validation of the EPSC predictions of the active deformation modes as a function of precipitates and solute content. The single-crystal elastic constants used for Mg were: $C_{11} = 56.3\ GPa$, $C_{12} = 24.6\ GPa$, $C_{13} = 20.7\ GPa$, $C_{33} = 58.2\ GPa$ and $C_{44} = 15.2\ GPa$.

In this study, we used a version of the EPSC model that calculates the hardening based on dislocation densities, which evolve during loading. This version is termed multi-scale (MS-EPSC) and is capable of treating the formation and growth of reoriented

deformation twin lamellae. The EPSC polycrystal model was first introduced by Turner and Tomé [50]. It applies the Eshelby inclusion formalism to represent each grain orientation and its interaction within a homogeneous effective medium (HEM), which embodies the bulk material. In addition, the MS-EPSC model used here includes the dislocation density based hardening model developed by Beyerlein and Tomé [51-52], which was extended further by Knezevic et al. [53]. It is capable of predicting the constitutive behavior during strain path changes by including the effects of reverse dislocation motion and de-twinning on strain hardening and texture evolution. In several prior studies, the constitutive model has been used within the VPSC framework for a variety of metals of different crystal structures: HCP Zr [54-56], Be [57], and Mg [58, 59], BCC Ta [60], BCC Nb [61], FCC superalloy Haynes [62] and orthorhombic uranium [63-65]. Its formulation is fully described in the above-cited works, while a very brief summary is given below.

Within the applied hardening model, the resistance to slip τ_c^s, is calculated using Eq. 2:

$$\tau_c^s = \tau_{o,f}^s + \tau_{0,HP}^s + \tau_{for}^s + \tau_{sub}^s. \quad (2)$$

It includes a friction stress $\tau_{o,f}^S$ (dependent on the Peierls stress and the initial content of dislocations), a barrier term $\tau_{o,HP}^S$ (dependent on initial grain size) and two terms that evolve with strain i.e., the forest and debris interaction stresses τ_{for}^s and τ_{sub}^S (dependent on a spatially random and ordered distribution of stored dislocations, respectively). The Hall-Petch effect is included using the grain-size dependent barrier effect term $\tau_{0,HP}^s$:

$$\tau_{0,HP}^{s} = \mu^{s} H^{s} \sqrt{\frac{b^{s}}{d_{g}}} \tag{3}$$

where μ^s is the effective shear modulus taken to be the same for each slip systems, *s*, H^s the Hall-Petch parameter, b^s the value of the Burgers vector and d_g the grain size. As twin boundaries introduce additional barriers, the grain-size term is replaced by the mean-free-path d_{mfp} between adjacent twin boundaries, i.e., $\tau_{0,HP}^{s} = \mu^{s} H^{s} \sqrt{\frac{b^{s}}{d_{mfp}}}$, when twins are present [66]. The evolution of the forest dislocation interaction stress τ_{for}^{s} and the dislocation substructure interaction stress τ_{sub}^{s} are based on the extended Taylor-type law [51, 53, 67]:

$$\begin{aligned} \tau_{for}^{s} &= \chi^{s} b^{s} \mu^{s} \sqrt{\rho_{for}^{s}}, \\ \tau_{sub}^{s} &= k_{sub} b^{s} \mu^{s} \sqrt{\rho_{sub}} \log\left(\frac{1}{b^{s}\sqrt{\rho_{sub}}}\right). \end{aligned} \tag{4}$$

Here, χ^s is a dislocation interaction parameter taken to be 0.9 for each slip system *s*, k_{sub} = 0.086 is a mathematical constant [53, 68, 69] and ρ_{for}^{s} and ρ_{sub}^{s} are the forest and substructure dislocation densities, respectively. The initial values of dislocation density were assumed to be 1.5 x 10^{12} m^{-2} for forest and 0.1 m^{-2} for substructure approximating the initial state of the material. The forest density evolves according to

$$\frac{\partial \rho_{for}^{s}}{\partial \gamma^{s}} = \frac{\partial \rho_{gen,for}^{s}}{\partial \gamma^{s}} - \frac{\partial \rho_{rem,for}^{s}}{\partial \gamma^{s}} = k_1^{s}\sqrt{\rho_{for}^{s}} - k_2^{s}(\dot{\varepsilon},T)\rho_{for}^{s},$$
$$\Delta\rho_{for}^{s} = \frac{\partial \rho_{for}^{s}}{\partial \gamma^{s}}|\Delta\gamma^{s}| \tag{5}$$

where γ^s is the shear strain, $\frac{\partial \rho_{gen,for}^{s}}{\partial \gamma^{s}}$ is the rate of dislocation generation (or storage), $\frac{\partial \rho_{rem,for}^{s}}{\partial \gamma^{s}}$ the rate of dislocation removal, k_1^s is a rate-insensitive coefficient, which accounts for dislocation storage due to statistical trapping of glide dislocations by forest obstacles and k_2^s a rate-sensitive coefficient for dynamic recovery by thermally activated mechanisms [51, 53, 70]. According to [51], k_2^s is calculated via:

$$\frac{k_2^s}{k_1^s} = \frac{\chi^s b^s}{g^s}\left(1 - \frac{kT}{D^s (b^s)^3}\ln\left(\frac{\dot{\varepsilon}}{\dot{\varepsilon}_0}\right)\right) \tag{6}$$

with k, $\dot{\varepsilon}$, $\dot{\varepsilon}_0 = 1 \cdot 10^7$, g^s and D^s being Boltzmann's constant, the applied strain rate, a reference strain rate, an effective activation enthalpy and a drag stress, respectively.

Twinning is modeled using the composite grain model developed by Proust et al. [66], while the initial stress and strain state within the twins is determined using the finite initial fraction (FIF) assumption [71]. The twin activation stress, τ_c^t, includes a temperature-independent friction term τ_0^t, a Hall-Petch-like barrier term, $\tau_{o,HP}^t$, and a latent hardening term coupling slip and twin systems. Similar to slip, the Hall-Petch-like term for twinning is $\tau_{o,HP}^t = \frac{HP^\beta}{\sqrt{d_g}}$ for grain boundaries and is $\tau_{HP}^t = \frac{HP^\beta}{\sqrt{d_{mfp}^t}}$ for twin boundary effects. The latent hardening term coupling slip and twin systems is $\mu^t \sum_t C^{st} b^t b^s \rho_{for}^s$ [53] and hence τ_c^t is calculated via:

$$\tau_c^t = \tau_o^t + \tau_{o,HP}^t + \mu^t \sum_t C^{st} b^t b^s \rho_{for}^s. \tag{7}$$

Consistent with experimental observations, we considered three slip modes and one twinning mode in our calculations. The slip modes made available to the alloys are the <a> slip modes prismatic $\{1\bar{1}00\}\langle 11\bar{2}0\rangle$ and basal $\{0001\}\langle 11\bar{2}0\rangle$ slip as well as <c+a> pyramidal $\{11\bar{2}2\}\langle 11\bar{2}\bar{3}\rangle$ slip. In addition, TTW-ing is included in our simulations.

In MS-EPSC, a polycrystal is represented with a set of grains (each having an orientation, shape and a volume fraction) representative of the material. Crystal orientations are defined using Bunge-Euler angles. Weights to individual crystal orientations are assigned to represent the initial texture of the material The discrete texture files were generated by calculating the orientation distribution functions (ODFs) from the recorded EBSD maps using the EDAX OIM™ Data Analysis software and importing them into the MTEX software package [72], which is capable of producing the required input texture data file. It is possible that the conversion from the calculated ODF into the polycrystal data file can cause the loss of some information. To check for deviations, we compared the inverse pole figures of the measured initial textures and the converted polycrystal data file used in the model and found a good match.

In the simulations, we applied homogeneous boundary conditions generating uniaxial compression/tension stresses in the prescribed load direction (relative to the initial texture) and traction-free surfaces in the other orthogonal directions.

5. Modeling results

In order to characterize the model parameters, the flow curves (Fig. 8), elastic lattice strains (Fig. 9-10) and texture evolution (Fig. 11) were evaluated and will be discussed in turn below. As shown, good agreement is achieved between the experimental data and modeling results. The corresponding hardening parameters for the slip and twinning modes are given in Table 1 and Table 2. In addition values for the finite initial fraction

(FIF) of 0.015 and HP^{β} of 145 for TTW-ing were established. The Burgers vector for tensile twinning is b^{ttw} = 5.54 ·10^{-11}m

5.1 Activation stresses and energies

As presented in Tables 1 and 2, we were able to characterize the slip and twin activation stresses and energies separately for the as-extruded, age-hardened and annealed samples. The spread in grain size of 17 to 20 µm was too small to accurately determine the Hall-Petch coefficients. Therefore, we used Hall-Petch coefficients, which were determined previously in Mg-Li(-Al) alloys featuring a wide spread in grain size [73]. Unfortunately, the strength increment between the as-extruded and the 16 h age hardened sample is too small to detect changes in the hardening parameters. However several important findings could be obtained.

First, as shown in Table 1, the slip activation stresses $\tau_{o,f}^{s}$ increase in the following order for all morphologies and volume fraction of precipitates: <a> basal < <a> prismatic < <c+a> pyramidal slip, as might be expected for Mg alloys. In agreement with Agnew et al. [25], we observe that age hardening has a significant effect on <a> basal slip, as can be seen by the relative increase of 50 % in $\tau_{o,f}^{s}$ between the as-extruded and the 500 h age hardened samples compared to the very slight changes in $\tau_{o,f}^{s}$ for <a> prismatic and <c+a> pyramidal slip.

Second, we find that the limited TTW-ing activity in the as-extruded and 16 h age hardened conditions (see section 3.2, Fig. 6 and [37]) is correlated with a remarkably high τ_{o}^{t} in these samples, where τ_{o}^{t} is in the order of $\tau_{o,f}^{s}$ for <c+a> pyramidal slip. This is significantly higher than that previously reported in WE43 [25], in WE54 [37] and AZ31 [71], where τ_{o}^{t} is similar to the $\tau_{o,f}^{s}$ of <a> prismatic slip. Here, it is important to

emphasize that τ_o^t is considerably lower in the 500 h age hardened and the 400 °C annealed samples, where the solute concentration has dropped. Thereby, we confirm an important hardening of TTW-ing by solutes as has been suggested in [37] and [38]. Stanford et al [38] explained the reduced TTW activity in binary Mg-Y alloy by the significant difference of the atomic radius of Y (0.181 nm [74]) in comparison to Mg (0.160 nm [74]). Likewise Nd features an atomic radius (0.182 nm [74]), which is very similar to Y and hence is likely to hinder TTW-ing analogous to Y.

Third, we observe decreasing $\tau_{o,f}^s$ for all slip modes in the 400 °C annealed sample. The microstructure of this material features a reduced solute content in the grain interior and precipitate formation at the grain boundaries. The modeling results suggest that the reduction of the solute concentration causes a weaker solute hardening and lack of precipitates in the grain interior makes them ineffective in resisting dislocation glide. However, k_1^s for <c+a> pyramidal slip is increased in the 400 °C annealed sample. This parameter is related to the rate of dislocation storage during deformation. Based on previous work, we infer that its increase is likely connected to the decreasing Y and Nd solute concentrations. As stated earlier, Sandlöbes et al. [31-33] had suggested a heterogeneous source mechanism, which is supported by TEM and classical continuum elasticity-based dislocation theory in Agnew et al. [75], where intrinsic I_1 stacking faults act as a heterogeneous source for <c+a> dislocations. Stacking faults formation would be hindered if the stacking fault energy were to increase by decreasing Y and Nd additions.

5.2 Lattice strain evolution

To add to the prior evaluation by EPSC, the elastic lattice strains as well as the EPSC prediction provide valuable insight into the contributions of slip and twinning

underlying the deformation behavior of these two alloys. Fig. 9 and 10 depict the evolution of axial and transversal elastic lattice strain of the $(10\bar{1}0)$, (0002), $(10\bar{1}1)$, $(10\bar{1}2)$, $(11\bar{2}0)$, $(10\bar{1}3)$, $(11\bar{2}2)$ and $(20\bar{2}1)$ reflections during compression and tension tests. Each reflection corresponds to a subset of grains, which feature a common orientation. Grains belonging to a $(10\bar{1}1)$, $(10\bar{1}2)$, $(10\bar{1}3)$ or $(11\bar{2}2)$ orientation possess high Schmid factors (SF) for <a> basal slip and relatively high SFs for <a> prismatic slip. As suggested by the model, these slip modes have the lowest $\tau_{o,f}^{s}$ and consequently, these reflections would be expected to feature the lowest axial and transversal elastic lattice strains in tension and compression tests.

The axial $(10\bar{1}0)$, $(11\bar{2}0)$ and $(20\bar{2}1)$ as well as the transversal (0002) reflections correspond to the $<10\bar{1}0>/<11\bar{2}0>$ texture components and hence possess high SF for <a> prismatic and <c+a> pyramidal slip as well as TTW-ing in case of compression loading. However, the SF for <a> basal slip is close to zero in these grains. In most Mg alloys such grains would deform by <a> prismatic slip and TTW-ing, where TTW-ing is readily activated when the compression direction is parallel to the extrusion direction (ED) and therefore, perpendicular to the crystallographic c-axis. A tension-compression yield asymmetry is generated since the TTW-ing is absent during tension tests parallel to ED, because here, the c-axis is aligned perpendicular to the external load resulting in c-axis compression. However, in the present alloy, we find via the modeling that TTW-ing has a very high activation threshold stress, $\tau_{o,f}^{s}$, and therefore, would likely occur after large strains. Hence, the deformation should initially be realized by slip. This notion is confirmed by the late occurrence of the axial (0002) reflection particularly in the as-extruded and the 16 h 250 °C sample. This reflection corresponds to twinned grains, which have been reoriented by TTW-ing (86° rotation about an $<11\bar{2}0>$ axis).

The onset of the (0002) reflection is shifted to lower strains in the 500 h 250 °C and the 24 h 400 °C compression samples, where TTW-ing is less hindered by the solutes.

The onset of twinning has been reported to generate a significant back-stress particularly in the (0002) oriented grains [71]. However, in the present alloy, TTW-ing is delayed and spread over a higher strain range, which results in the absence of a significant back-stress. In addition, the twinned grains (generating (0002) reflections) being aligned with their c-axis close to the loading axis feature low SFs for <a> basal slip, <a> prismatic slip and TTW-ing and hence require the activation of <c+a> pyramidal slip. Usually, the necessity of high relative activities of <c+a> pyramidal slip within the twinned grains results in pronounced hardening, which is observed via a sigmoidal compression flow curve as well as a significant increase of the elastic lattice strains. However, such features are absent in the present WE54 alloy, where the (0002) oriented grains exhibits very limited hardening. Therefore, we conclude that <c+a> pyramidal slip occurs at a relatively low CRSS (Table 1, $\tau_{0,f}^{s}$), a finding consistent with TEM investigations and first-principle calculations [31-33].

5.3 Texture evolution and deformation mode activity

Based on the conducted experiments and EPSC simulations, the relative deformation mode activity associated with the observed texture development can be extracted. A comparison of the simulated (Fig. 11) and the experimental textures (Fig. 5) displays good agreement. The only minor deviation occurs at -5% compression, where the simulated inverse pole figures show a <0002> texture component unlike the measured pole figures. We attribute these discrepancies between the measured and simulated textures to the approximation of the mean-field self-consistent homogenization scheme, which takes into account grain-to-grain interactions only in an average sense without

explicit neighboring effects. Therefore any large fluctuation in the local stress fields caused by grain-to-grain interactions is reduced. These local effects are known to affect twin variant selection and delay twin propagation [59, 76]. Since these effects are not considered within the present model, twinning happen earlier causing faster texture evolution. The predicted TTW volume fractions are only slightly higher than the measured TTW volume fractions, showing reasonably accurate predictions of TTW activity.

Fig. 12 depicts the relative deformation mode activity as a function of the applied strain path and strain. It is evident that TTW-ing is significantly hindered compared to other Mg alloys, such as AZ31 [71] or ME21 [16, 37] particularly in the as-extruded and the 16 h age hardened samples. The reduced TTW activity has to be compensated by the enhanced activation of slip. Here, we find that <a> prismatic slip and <a> basal slip are particularly enhanced, while an enhancement of <c+a> pyramidal slip at low compressive strains is only predicted in the as-extruded and the 16 h 250 °C samples. The 500 h age-hardened and 400 °C annealed samples feature a higher TTW activity in comparison to the other materials conditions and consequently, a reduced initial activity of <c+a> pyramidal slip. Tensile deformation is predominantly realized by <a> prismatic and <a> basal slip. The activation of these <a> slip modes causes the enhancement of the $<10\bar{1}0>$ texture component. In addition, in tension, we predict a small relative activity of the <c+a> pyramidal slip system. Thereby, our simulations confirm an enhancement of <c+a> pyramidal slip and pronounced hardening of TTW-ing by Y and Nd solutes.

6. Conclusions

The deformation behavior of as-extruded, age-hardened, and annealed WE54 samples was investigated using tension and compression tests, EBSD and in-situ elastic lattice strain measurements by energy-dispersive X-ray synchrotron diffraction in combination with detailed crystal plasticity modeling using the multi-scale elasto-plastic self-consistent (MS-EPSC) model. Based on our results and those from the current literature, the following conclusions can be drawn:

- The WE54 alloy exhibits an uncommonly low $\{10\bar{1}2\}\langle 10\bar{1}\bar{1}\rangle$ tension twinning activity particularly in the as-extruded and 16 h 250 °C age hardened conditions.
- The tension twinning activity increases after age-hardening for 500 h at 250 °C and for 24 h at 400 °C. These heat treatments were found to reduce the solute concentrations of Y and Nd and form precipitates within the grain interior or the grain boundaries. The analyses indicate that precipitate formation at the grain boundaries does not harden slip via all three modes considered here (basal <a>, prismatic <a>, and pyramidal <c+a> slip). Consequently, the enhanced tension twinning activity observed in the 400 °C annealed samples cannot be attributed to selective hardening of slip, but to reduced solute concentrations.
- The plate-shaped precipitates, which form on prismatic planes during 250 °C age hardening, have a more significant hardening effect on <a> basal slip than on other slip modes.
- The reduced TTW activity due to solutes is compensated for by enhanced activation of slip, where <a> prismatic slip and <a> basal slip activity are particularly increased.

- High solute concentrations of Y and Nd appear to enhance <c+a> pyramidal slip especially during tensile testing (as-extruded and 16 h 250°C samples)

Acknowledgements
M. Lentz and W. Reimers are grateful for the financial support of the Deutsche Forschungsgemeinschaft (DFG) under the contract number RE 688/67-1. M. Knezevic and M. Zecevic were supported by a U.S. National Science Foundation grant CMMI-1301081. I.J. Beyerlein gratefully acknowledges support by a Laboratory Directed Research and Development project 20140348ER. The authors would like to thank Katrin Brömmelhoff, Alexander Treff and Christoph Seyfert (TU Berlin, Metallische Werkstoffe) for the support of the in-situ experiments, Sören Selve (TU Berlin, ZELMI) for conducting the HR-TEM analysis and Jörg Nissen (TU Berlin, ZELMI) for conducting the EPMA analysis.

References

[1] E.W. Kelley, W.F. Hosford, Trans. Metall. Soc. AIME 242 (1968) 5-13.

[2] X.Y. Lou, M. Li, R.K. Boger, S.R. Agnew, R.H. Wagoner, Int. J. Plast. 23 (2007) 44-86.

[3] S.R. Agnew, C.N. Tomé, D.W. Brown, T.M. Holden, S.C. Vogel, Scripta Mater. 48 (2003) 1003-1008.

[4] S.R. Agnew, Ö. Duygulu, Int. J. Plast. 21 (2005) 1161-1193.

[5] S.R. Agnew, D.W. Brown, C.N. Tomé, Acta Mater. 54 (2006) 4841-4852.

[6] M.R. Barnett, Mater. Sci. Eng. A 464 (2007) 1-7.

[7] M.R. Barnett, Z. Keshavarz, A.G. Beer, D.G. Atwell, Acta Mater. 52 (2004) 5093-5103.

[8] J.A. del Valle, F. Carreño, O.A. Ruano, Acta Mater 54 (2006) 4247-4259.

[9] P. Dobroň, F. Chmelík, S.B. Yi, K. Parfenenko, D. Letzig, J. Bohlen, Scripta Mater. 65 (2011) 424-427.

[10] A. Jain, O. Duygulu, D.W. Brown, C.N. Tomé, S.R. Agnew, Mater. Sci. Eng. A 486 (2008) 545-555.

[11] M.R. Barnett, Scripta Mater. 59 (2008) 696-698.

[12] J. Bohlen, M.R. Nürnberg, J.W. Senn, D. Letzig, S.R. Agnew, Acta Mater. 55 (2007) 2101-2112.

[13] R. Gehrmann, M.M. Frommert, G. Gottstein, Mater. Sci. Eng. A 395 (2005) 338-349.

[14] H. Wang, P.D. Wu, M.A. Gharghouri, Mater. Sci. Eng. A 527 (2010) 3588-3594.

[15] S. Gall, R.S. Coelho, S. Müller, W. Reimers, Mater. Sci. Eng. A 579 (2013) 180-187.

[16] M. Lentz, M. Klaus, W. Reimers, B. Clausen, Mater. Sci. Eng. A 586 (2013) 178-189.

[17] J.F. Nie, Scripta Mater. 48 (2003) 1009-1015.

[18] J.D. Robson, N. Stanford, M.R. Barnett, Scripta Mater. 63 (2010) 823-826.

[19] J.D. Robson, N. Stanford, M.R. Barnett, Acta Mater. 59 (2011) 1945-1956.

[20] J.D. Robson, N. Stanford, M.R. Barnett, Metall. Mater. Trans. A 44 (2013) 2984-2995.

[21] J. Robson, Metall. Mater. Trans. A 45 (2014) 5226-5235.

[22] N. Stanford, M.R. Barnett, Mater. Sci. Eng. A 516 (2009) 226-234.

[23] N. Stanford, J. Geng, Y.B. Chun, C.H.J. Davies, J.F. Nie, M.R. Barnett, Acta Mater. 60 (2012) 218-228.

[24] J.F. Nie, Metall. Mater. Trans. A 43 (2012) 3891-3938.

[25] S.R. Agnew, R.P. Mulay, F.J. Polesak III, C.A. Calhoun, J.J. Bhattacharyya, B. Clausen, Acta Mater. 61 (2013) 3769-3780.

[26] A. Akthar, E. Teghtsoonian, Acta Metall. Mater. 17 (1969) 1339-1349.

[27] A. Akthar, E. Teghtsoonian, Acta Metall. Mater. 17 (1969) 1351-1356.

[28] S.R. Agnew, M.H. Yoo, C.N. Tomé, Acta Mater. 49 (2001) 4277-4289.

[29] N. Stanford, M.R. Barnett, Int. J. Plast. 47 (2013) 165-181.

[30] N. Stanford, R. Cottam, B. Davies, J. Robson, Acta Mater. 78 (2014) 1-13.

[31] S. Sandlöbes, S. Zaefferer, I. Schestakow, S. Yi, R. Gonzalez-Martinez, Acta Mater. 59 (2011) 429-439.

[32] S. Sandlöbes, M. Friák, S. Zaefferer, A. Dick, S. Yi, D. Letzig, Z. Pei, L.-F. Zhu, J. Neugebauer, D. Raabe, Acta Mater. 60 (2012) 3011-3021.

[33] S. Sandlöbes, M. Friák, J. Neugebauer, D. Raabe, Mater. Sci. Eng. A 576 (2013) 61-68.

[34] J.F. Nie, B.C. Muddle, Scripta Mater. 40 (1999) 1089-1094.

[35] J.F. Nie, B.C. Muddle, Acta Mater. 48 (2000) 1691-1703.

[36] Y. Gao, H. Liu, R. Shi, N. Zhou, Z. Xu, Y.M. Zhu, J.F. Nie, Y. Wang, Acta Mater. 60 (2012) 4819-4832.

[37] M. Lentz, M. Klaus, R.S. Coelho, N. Schaefer, F. Schmack, W. Reimers, B. Clausen, Metall. Mater. Trans. A 45 (2014) 5721-5735.

[38] N. Stanford, R.K.W. Marceau, M.R. Barnett, Acta Mater. 82 (2015) 447-456.

[39] V. Herrera-Solaz, P. Hidalgo-Manrique, M.T. Pérez-Prado, D. Letzig, J. Llorca, J. Segurado, Materials Letters 128 (2014) 199-203.

[40] S. Sandlöbes, Z. Pei, M. Friák, L.-F. Zhu, F. Wang, S. Zaefferer, D. Raabe, J. Neugebauer, Acta Mater. 70 (2014) 92-104.

[41] Q. Zhang, T.W. Fan, L. Fu, B.Y. Tang, L.M. Peng, W.J. Ding, Intermetallics 29 (2012) 21-26.

[42] M.D. Abramoff, P.J. Magalhaes, S.J. Ram, Biophotonics Int. 11 (2004) 36–42.

[43] C. Genzel, I. Denks, J. Gibmeier, M. Klaus, G. Wagener, Nucl. Instrum. Meth. A 578 (2007) 23-33.

[44] E.A. Ball, P.B. Pragnell, Scripta Metall. Mater. 31 (1994) 111-116.

[45] M. Lentz, R.S. Coelho, B. Camin, C. Fahrenson, N. Schaefer, S. Selve, T. Link, I.J. Beyerlein, W. Reimers, Mater. Sci. Eng. A 610 (2014) 54-64.

[46] A.S. Khan, A. Pandey, T. Gnäupel-Herold, R.K. Mishra, Int. J. Plast. 27 (2011) 688–706.

[47] S. Kurukuri, M.J. Worswick, D.G. Tari, R.K. Mishra, J.T. Carter, Phil. Trans. R. Soc. A (2014), http://dx.doi.org/10.1098/rsta.2013.0216.

[48] M. Huppmann, M. Lentz, S. Chedid, W. Reimers, J. Mater. Sci. 46 (2011) 938-950.

[49] M. Knezevic, A. Levinson, R. Harris, R.K. Mishra, R.K. Doherty, S.R. Kalidindi, Acta Mater. 58 (2010) 6230-6242.

[50] P.A. Turner, C.N. Tomé, Acta Metall. Mater. 42 (1994) 4143-4153.

[51] I.J. Beyerlein, C.N. Tomé, Int. J. Plasticity 24 (2008) 867-895.

[52] I.J. Beyerlein, R.J. McCabe, C.N. Tomé, Journal of Multiscale Computational Engineering 9 (2011) 459-480.

[53] M. Knezevic, I.J. Beyerlein, D.W. Brown, T.A. Sisneros, C.N. Tomé, Int. J. Plast. 49 (2013) 185-198.

[54] M. Knezevic, I.J. Beyerlein, T. Nizolek, N.A. Mara, T.M. Pollock, Mater. Res. Lett. 1 (2013) 133-140.

[55] M. Knezevic, T. Nizolek, M. Ardeljan, I.J. Beyerlein, N.A. Mara, T.M. Pollock, Int. J. Plast. 57 (2014) 16-28.

[56] M. Ardeljan, I.J. Beyerlein, M. Knezevic, J. Mech. Phys. Solids 66 (2014) 16-31.

[57] M. Knezevic, I.J. Beyerlein, D.W. Brown, T.A. Sisneros, C.N. Tomé, Int. J. Plast. 49 (2013) 185-198.

[58] A.L. Oppedal, H. El Kadiri, C.N. Tomé, G.C. Kaschner, S.C. Vogel, J.C. Baird, M.F. Horstemeyer, Int. J. of Plast. 30-31 (2012) 41-61.

[59] I.J. Beyerlein, R.J. McCabe, C.N. Tomé, J. Mech. Phys. Solids 59 (2011) 988-1003.

[60] M. Knezevic, I.J. Beyerlein, M.L. Lovato, C.N. Tomé, A.W. Richards, R.J. McCabe, Int. J. Plast. 62 (2014) 93-104.

[61] M. Ardeljan, I.J. Beyerlein, M. Knezevic, J. Mech. Phys. Solids, 66 (2014) 16-31.

[62] M. Knezevic, J.S. Carpenter, M.L. Lovato, R.J. McCabe, Acta Mater. 63 (2014) 162-168.

[63] M. Knezevic, R.J. McCabe, R.A. Lebensohn, C.N. Tomé, C. Liu, M.L. Lovato, B. Mihaila, J. Mech. Phys. Solids 61 (2013) 2034-2046.

[64] M. Knezevic, R.J. McCabe, C.N. Tomé, R.A. Lebensohn, S.R. Chen, C.M. Cady, G.T. Gray III, B. Mihaila, Int. J. Plast. 43 (2013) 70-84.

[65] M. Knezevic, L. Capolungo, C.N. Tomé, R.A. Lebensohn, D.J. Alexander, B. Mihaila, R.J. McCabe, Acta Mater. 60 (2012) 702-715.

[66] G. Proust, C.N. Tomé, G.C. Kaschner, Acta Mater. 55 (2007) 2137-2148.

[67] H. Mecking, U.F. Kocks, Acta Metall. Mater. 41 (1981) 1865-1875.

[68] R. Madec, B. Devincre, L.P. Kubin, Phys. Rev. Lett. 89 (2002) 255508

[69] L. Capolungo, I.J. Beyerlein, G.C. Kaschner, C.N. Tomé, Mater. Sci. Eng. A 513-514 (2009) 42-51.

[70] M. Knezevic, I.J. Beyerlein, T. Nizolek, N.A. Mara, T.M. Pollock, Mater. Res. Lett. 2013; 1: 133-140.

[71] B. Clausen, C.N. Tomé, D.W. Brown, S.R. Agnew, Acta Mater. 56 (2008) 2456-2468.

[72] F. Bachmann, R. Hielscher, H. Schaeben, Solid State Phenom. 160 (2010) 63–68.

[73] M. Lentz M, M. Klaus, I.J. Beyerlein, M. Zecevic, W. Reimers, M. Knezevic, Acta Mater. accepted.

[74] J.F. Shackelford. Werkstofftechnologie für Ingenieure, sixth ed., Pearson Studium, 2005.

[75] S.R. Agnew, L. Capolungo, C.A. Calhoun, Acta Mater. 82 (2015) 255-265.

[76] S.R. Niezgoda, A.K. Kanjarla, I.J. Beyerlein, C.N. Tomé, Int. J. Plast. 56 (2014) 119-138.

Figure captions

Fig. 1: Optical micrographs showing the initial microstructure of a) as-extruded material, and heat treated material under the following time-temperature conditions b) 16h at 250°C, c) 500h at 250°C, d) 24h at 400°C.

Fig. 2: SEM images showing precipitates in a) as-extruded material, and heat treated material under the following time-temperature conditions b) 16 h at 250 °C, c) 500 h at 250 °C, d) 24 h at 400 °C.

Fig. 3: TEM images of precipitates in the heat treated material under the following time-temperature conditions a) 16h 250°C; <00.2> zone axis, b) 16h 250°C; <11.0> zone axis, c) 500h 250°C; <00.2> zone axis d) 500h 250°C; <11.0> zone axis

Fig. 4: Flow stress-strain curves of the studied material in a) compression, and b) tension.

Fig. 5: Inverse pole figures showing texture development during heat treatment and subsequent deformation.

Fig. 6: EBSD maps of deformed samples: a, d, g, j) at -5% compression; b, e, h, k) after final load step - compression; c, f, i, l) after final load step - tension

Fig. 7: Histograms showing misorientation distribution at -5% compression in a) as-extruded and heat treated material under b) 16 h at 250°C, c) 500 h at 250°C, d) 24 h at 400°C

Fig 8: Comparison of the experimental and simulated flow curves. The serrated shape of the experimental flow curves is due to relaxation process during the diffraction data acquisition.

Fig. 9: Comparison of the experimentally measured and predicted elastic lattice strains during compression.

Fig. 10: Comparison of the experimentally measured and predicted elastic lattice strains during tension. Due to the initial texture and the strain path the (0002) reflection could not be accurately measured and hence, the label “not available” was added.

Fig 11: Inverse pole figures showing the simulated textures (extrusion direction is load direction). The starting textures exhibit minor deviations from the measured textures, which are attributed to the conversion of the calculated ODF to the polycrystal data file.

Fig 12: Relative activities of the active deformation mode predicted by the model.

Table 1: Hardening parameters for slip.

	As-extruded			16 h 250 °C		
Parameter	s= 1 (<a> prismatic)	s = 2 (<a> basal)	s= 3 (<c+a> pyramidal)	s= 1 (<a> prismatic)	s = 2 (<a> basal)	s= 3 (<c+a> pyramidal)
$\tau_{0,f}^{s}$ (MPa)	80	10	115	80	10	115
k_1^s (m^{-1})	1.5E+08	1.0E+08	2.5E+09	1.5E+08	1.0E+08	2.5E+09
D^s (MPa)	3.5E+03	3.5E+03	8.5E+03	3.5E+03	3.5E+03	8.5E+03
g^s	5.0E-03	5.0E-03	9.5E-03	4.0E-03	4.0E-03	9.5E-03
H^S	160	90	20	160	90	20
C^{st}	50	50	400	50	50	400
	500 h 250 °C			24 h 400 °C		
Parameter	s= 1 (<a> prismatic)	s = 2 (<a> basal)	s= 3 (<c+a> pyramidal)	s= 1 (<a> prismatic)	s = 2 (<a> basal)	s= 3 (<c+a> pyramidal)
$\tau_{0,f}^{s}$ (MPa)	82	15	115	60	8	105
k_1^s (m^{-1})	1.5E+08	1.0E+08	8.5E+09	1.5E+08	1.0E+08	15.5E+09
D^s (MPa)	3.5E+03	3.5E+03	8.5E+03	3.5E+03	3.5E+03	8.5E+03
g^s	4.0E-03	4.0E-03	11.5E-03	4.0E-03	4.0E-03	7.5E-03
H^S	160	90	20	160	90	20
C^{st}	50	50	400	50	50	400

Table 2: Hardening parameters for TTW-ing (t =1).

Parameter	As-extruded	16 h 250 °C	500 h 250 °C	24 h 400 °C
τ_0^t (MPa)	115	115	98	78

Fig, 1

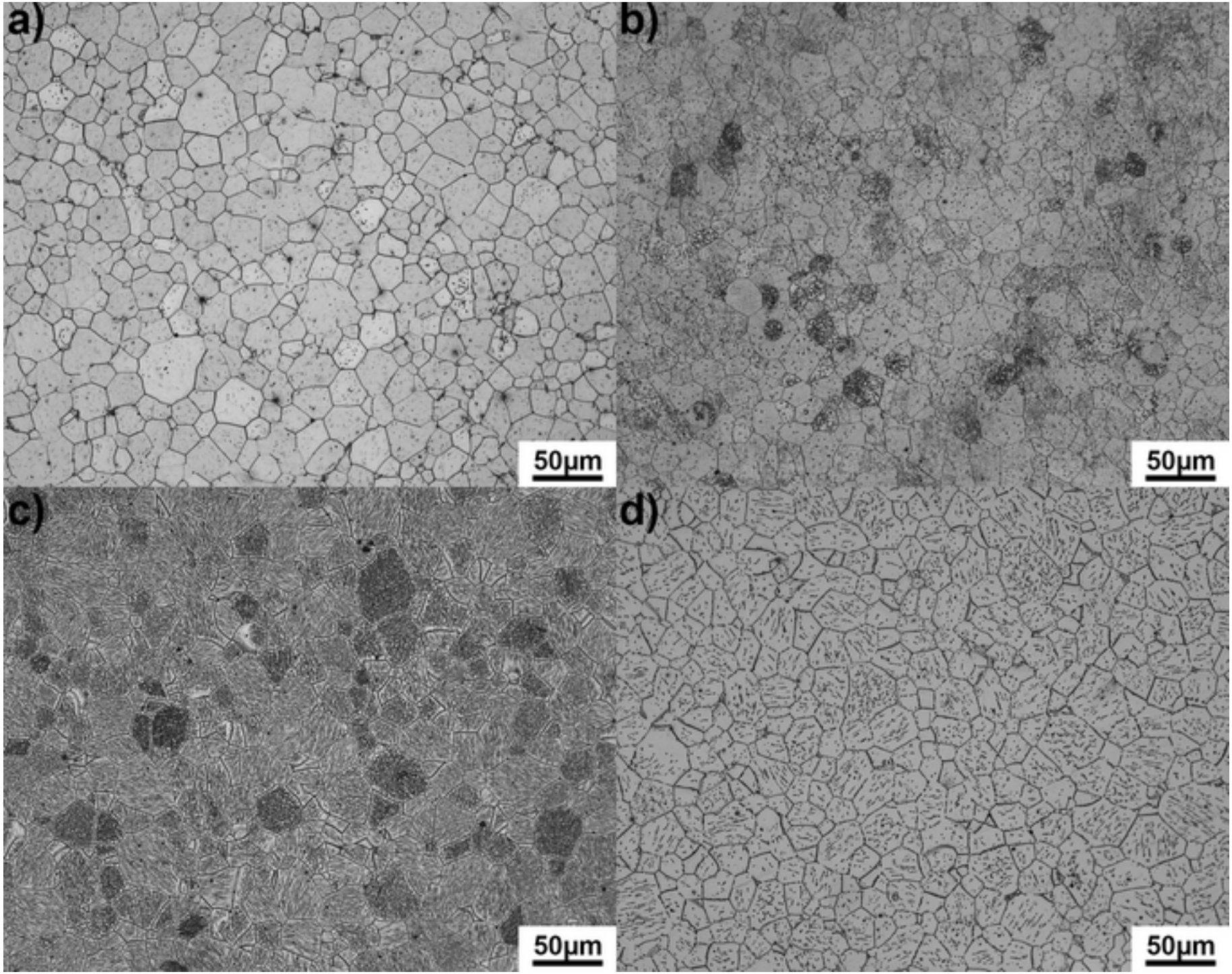

Fig, 2

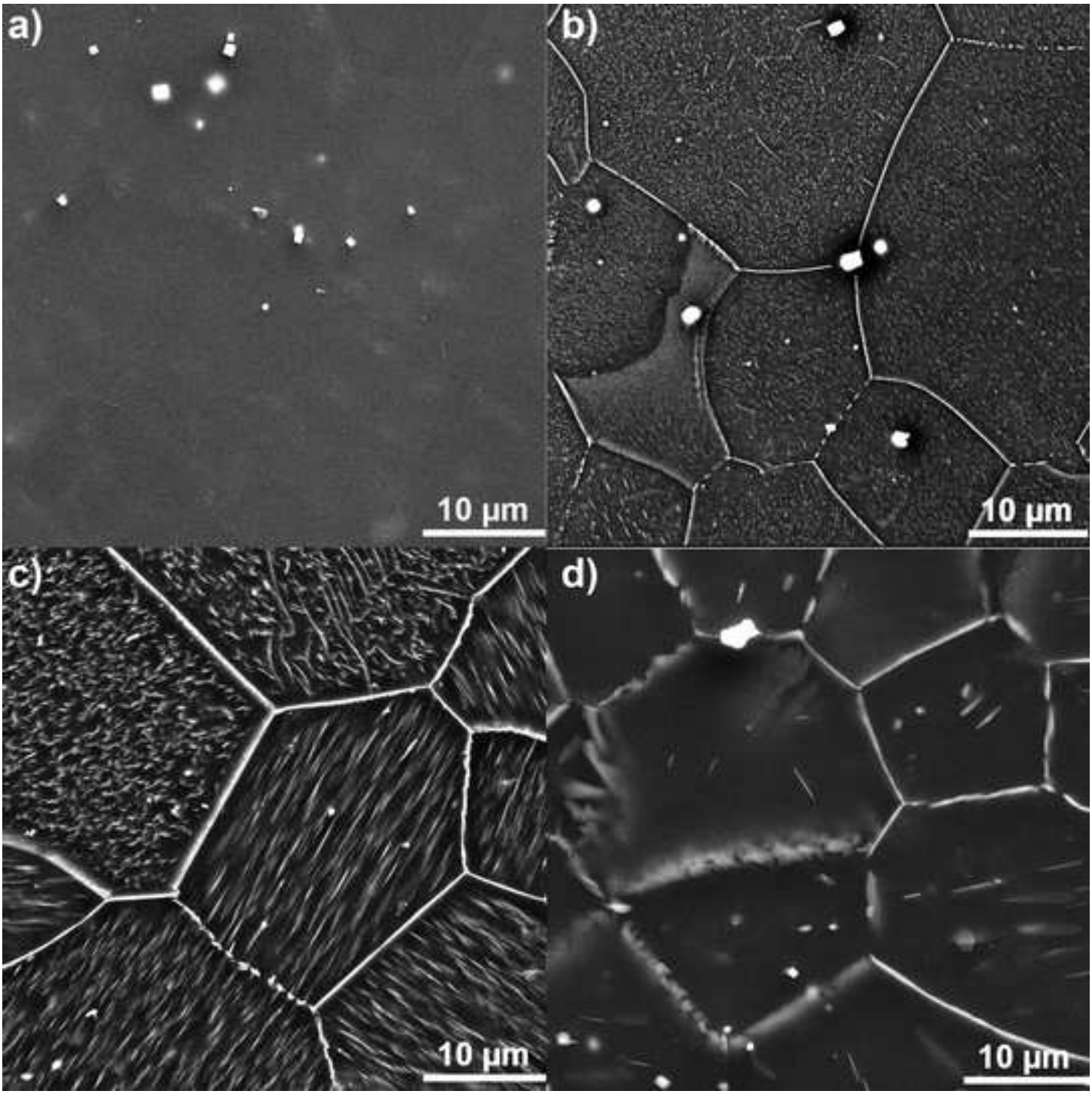

Fig, 3

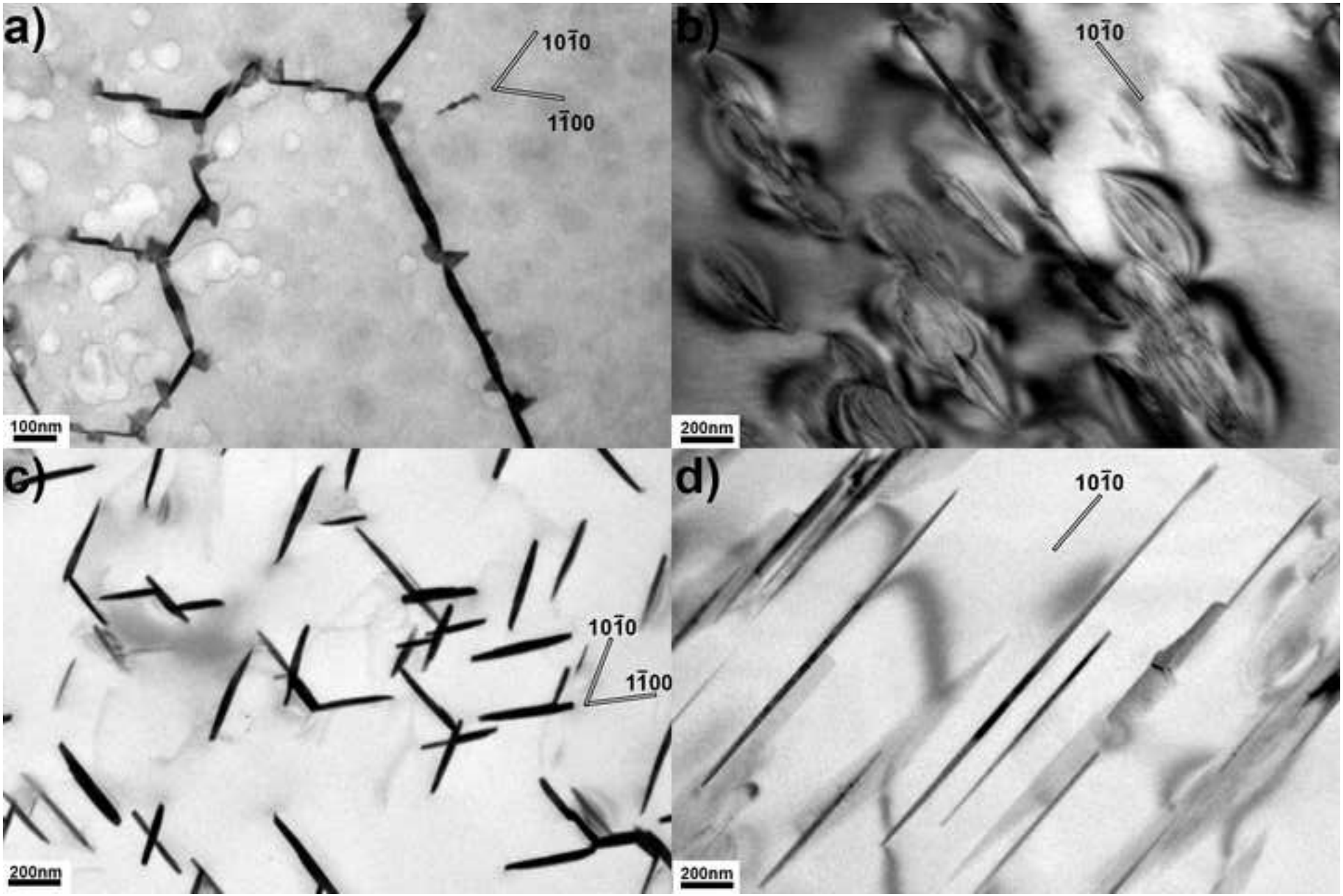

Fig, 4

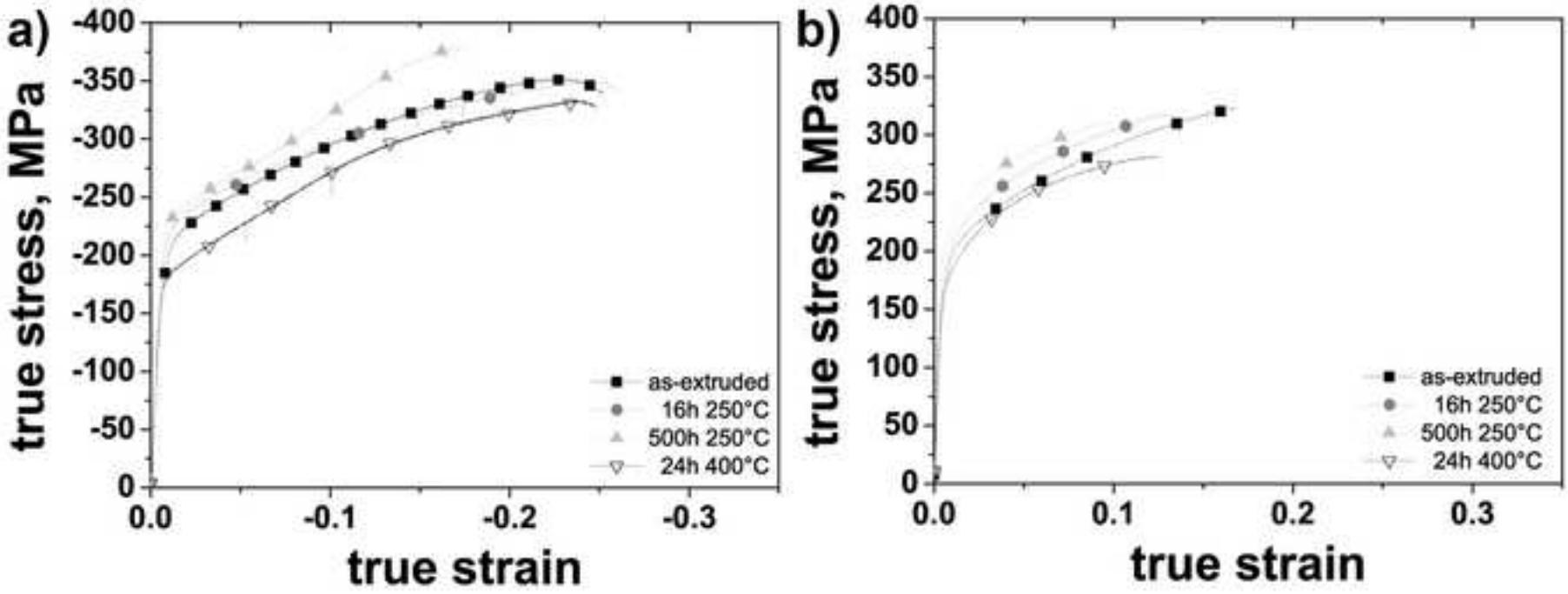

Fig, 5

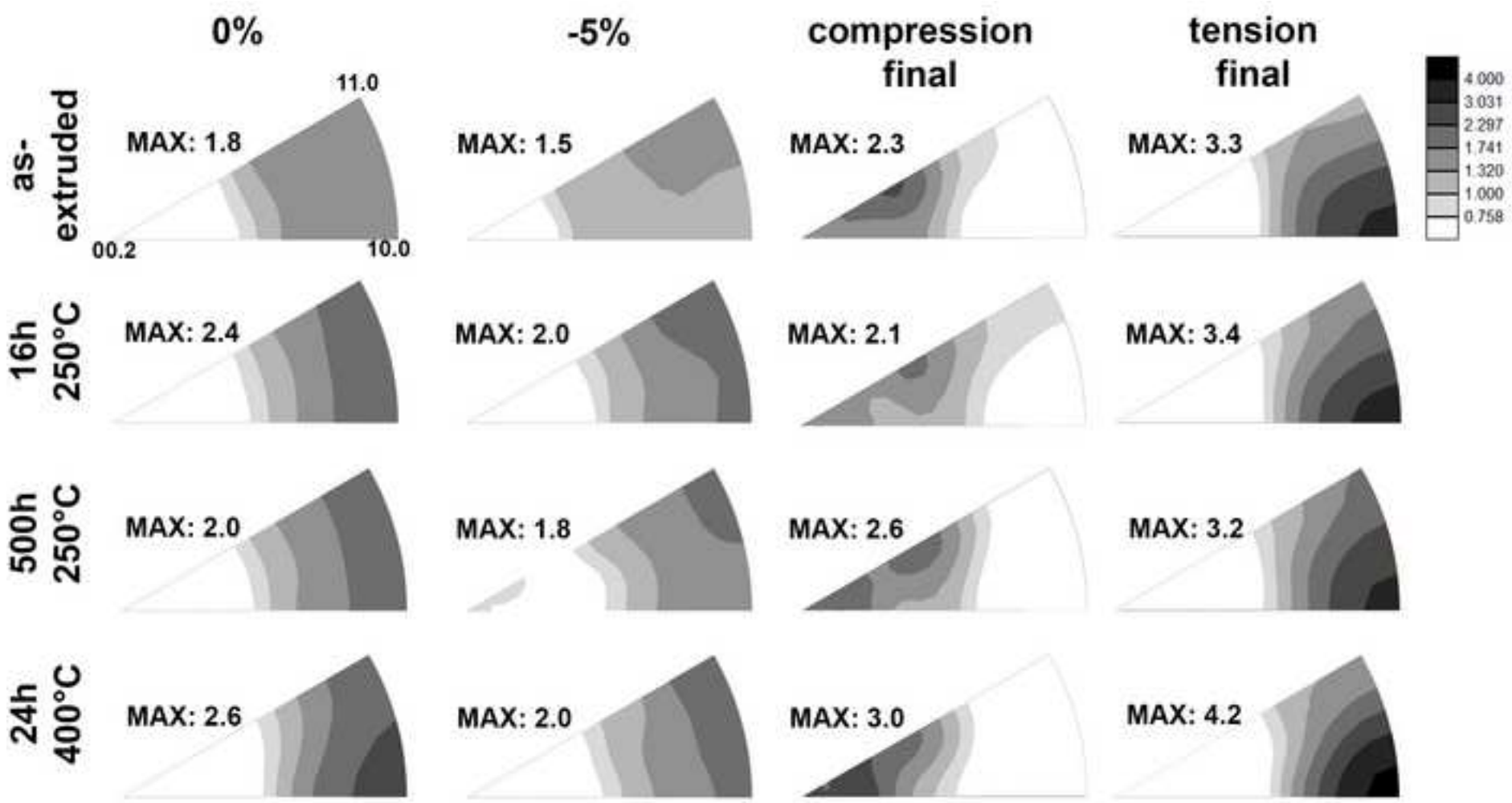

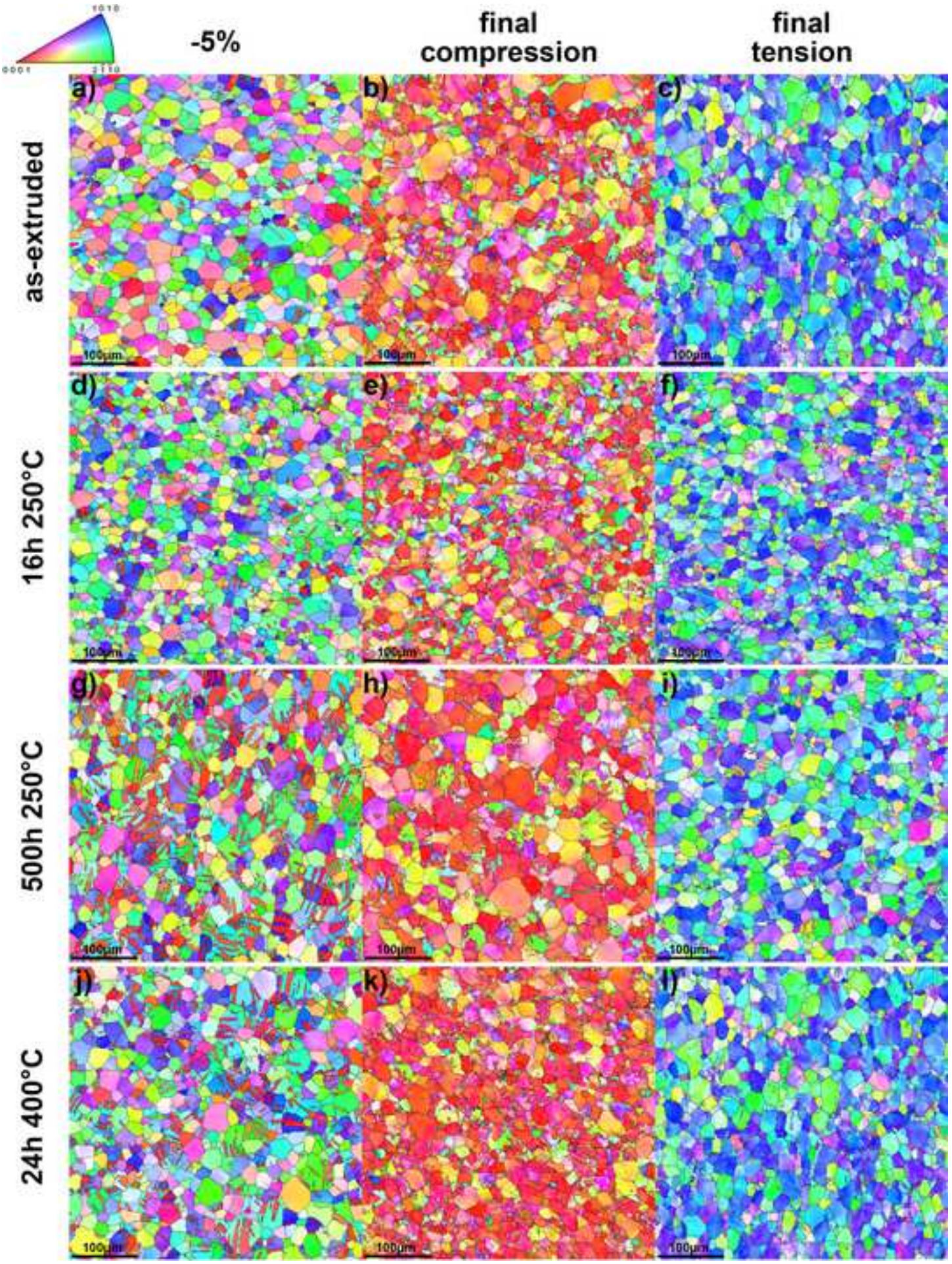

Fig, 7

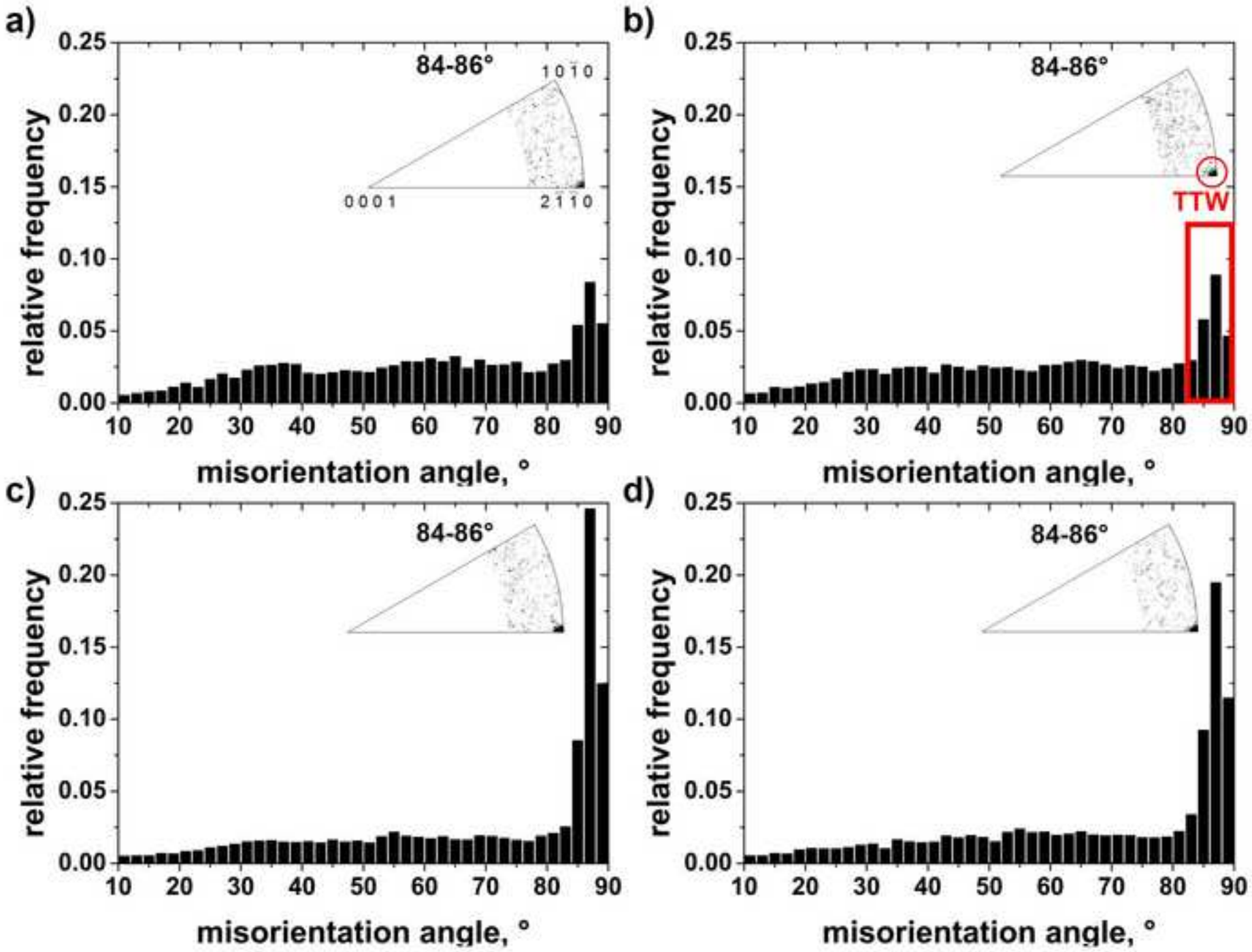

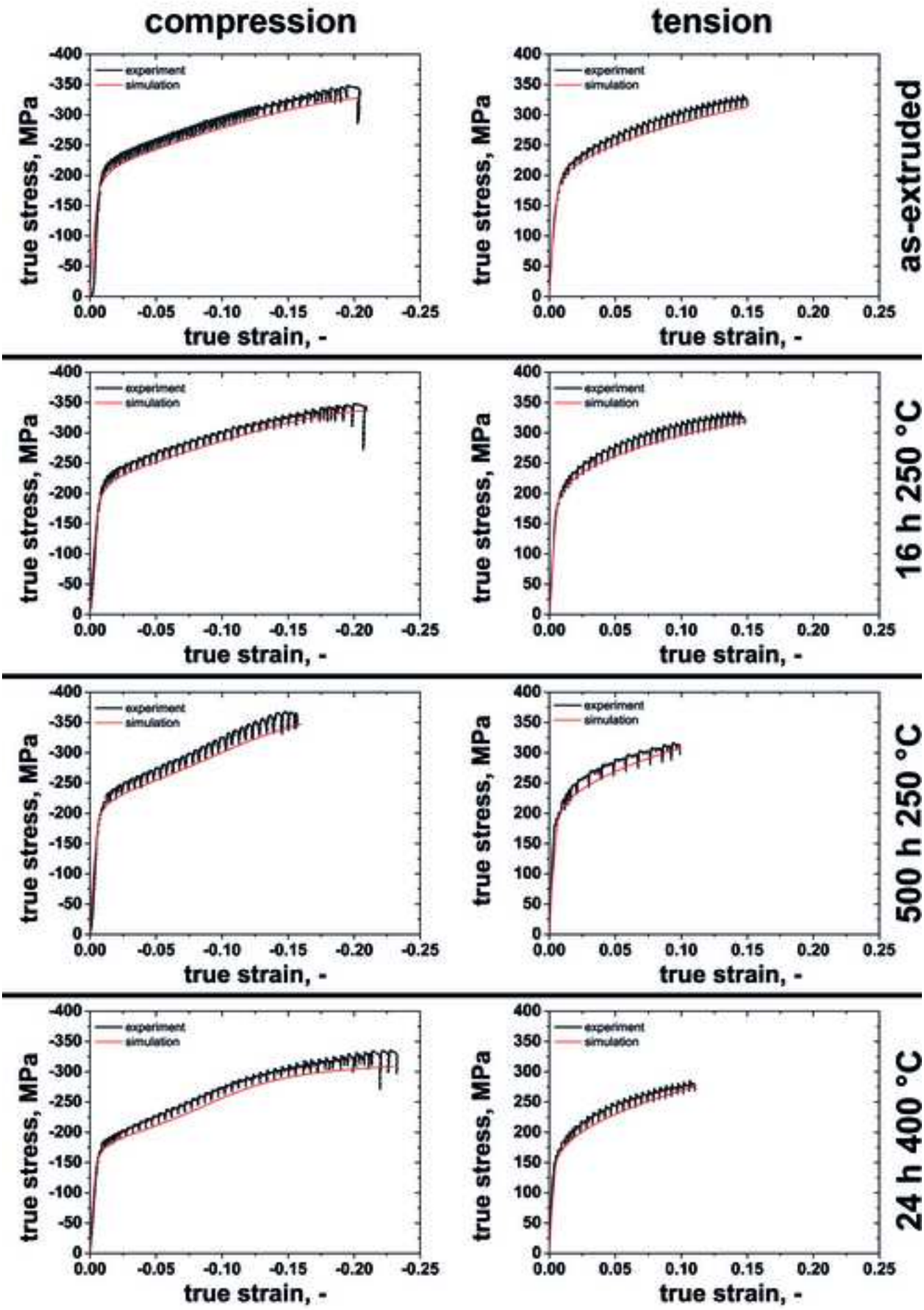

Fig, 9

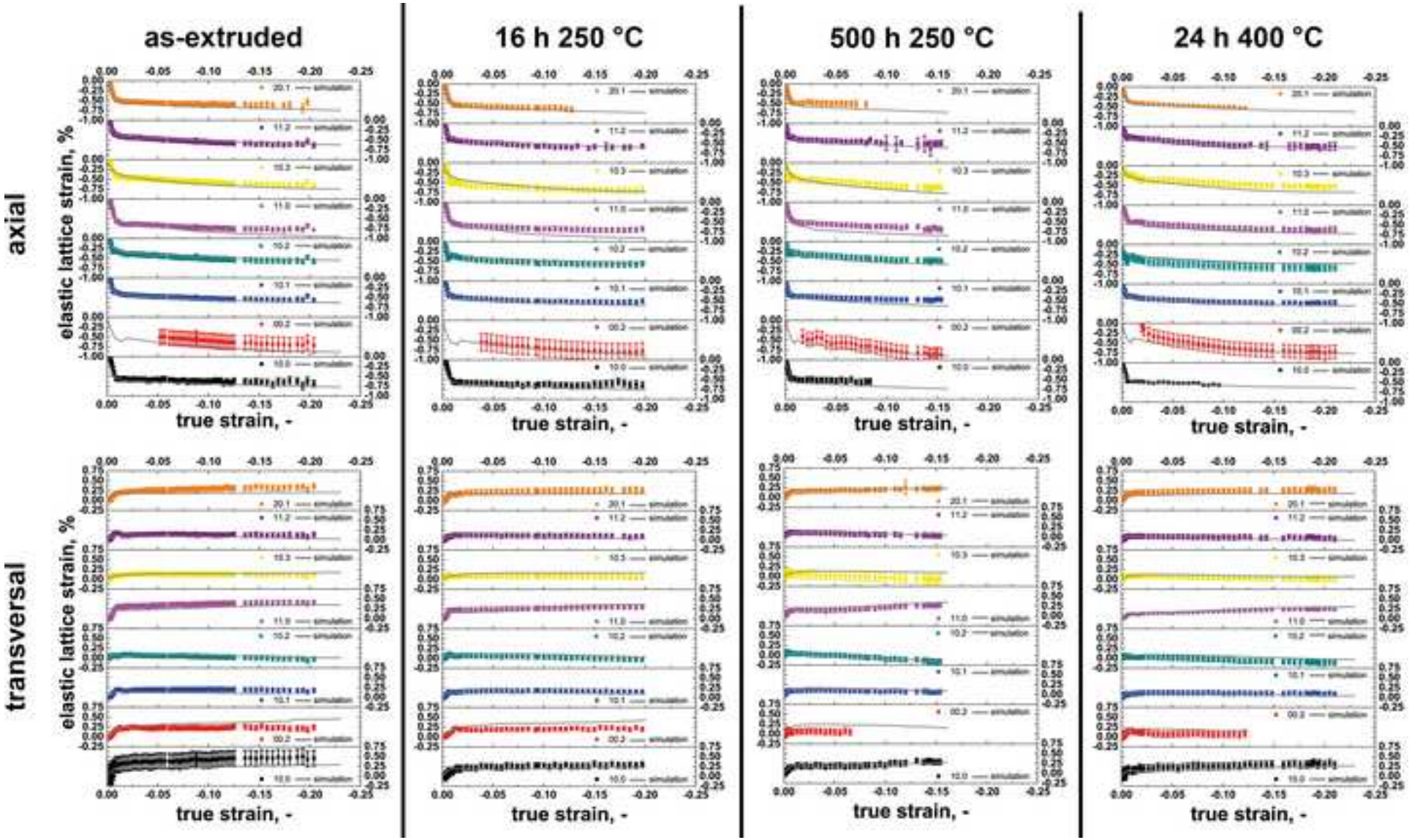

Fig, 10

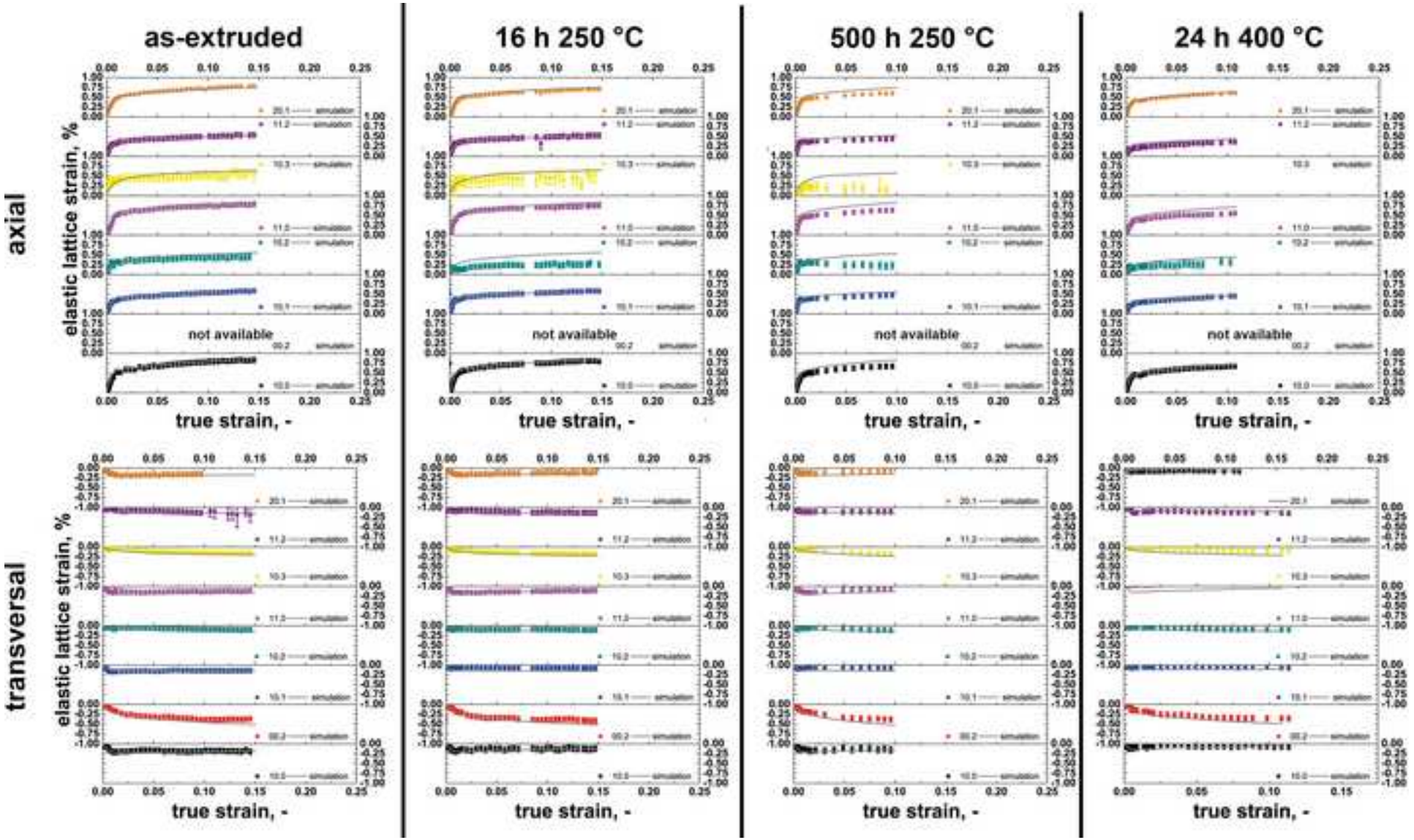

Fig, 11

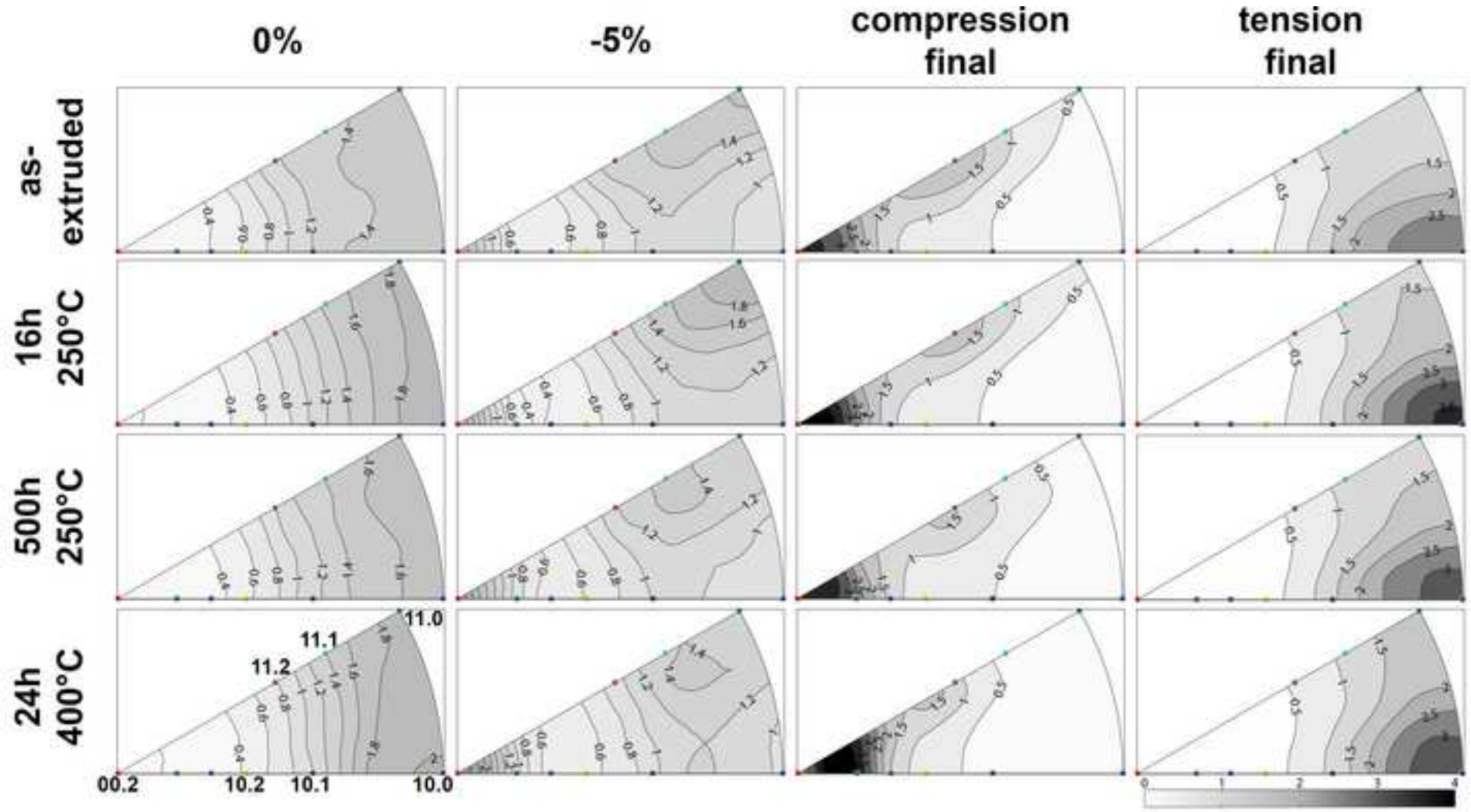

Fig, 12